Evolution of initial discontinuities in the Riemann problem for the Kaup-Boussinesq equation with positive dispersion

T. Congy,[1] S. K. Ivanov,[2,3] A. M. Kamchatnov,[2] and N. Pavloff[1]

[1]*LPTMS, CNRS, Univ. Paris-Sud, Université Paris-Saclay, 91405 Orsay, France*
[2]*Institute of Spectroscopy, Russian Academy of Sciences, Troitsk, Moscow 108840, Russia*
[3]*Moscow Institute of Physics and Technology, Institutsky lane 9, Dolgoprudny, Moscow region 141700, Russia*

We consider the space-time evolution of initial discontinuities of depth and flow velocity for an integrable version of the shallow water Boussinesq system introduced by Kaup. We focus on a specific version of this "Kaup-Boussinesq model" for which a flat water surface is modulationally stable, we speak below of "positive dispersion" model. This model also appears as an approximation to the equations governing the dynamics of polarisation waves in two-component Bose-Einstein condensates. We describe its periodic solutions and the corresponding Whitham modulation equations. The self-similar, one-phase wave structures are composed of different building blocks, which are studied in detail. This makes it possible to establish a classification of all the possible wave configurations evolving from initial discontinuities. The analytic results are confirmed by numerical simulations. *Published by AIP Publishing.* [http://dx.doi.org/10.1063/1.4997052]

The Kaup-Boussinesq (KB) water wave equation is integrable, but its generic form suffers from a dynamical instability. We study here the Riemann problem for a version of this equation, which does not suffer from the same deficiency. This equation appears as an approximation of the nonlinear polarization dynamics of a two-component Bose-Einstein condensate, and in this context, it is important to characterize the time evolution of simple, but experimentally relevant initial profiles.

I. INTRODUCTION

In many physical wave systems, the initial value problem treated in the long-wavelength (hydrodynamic) approximation leads to wave breaking after a finite time. As a result, the formal solution becomes multivalued, i.e., it looses its physical meaning. At the wave breaking point, the first spatial derivative of the physical variables diverges and the hydrodynamic approximation fails. This suggests that this nonphysical behavior can be remedied by accounting for physical effects described by terms with higher-order derivatives in the corresponding evolution equations. For example, within the Navier-Stokes description of the dynamics of a compressible gas, the effects of viscosity are described by second-order derivative terms, and this leads, instead of wave breaking, to the formation of viscous shocks, which can often be formally described by surfaces of discontinuities in the physical variables. Formulated in this way, the theory of "shock waves" has found a number of important applications.[1,2]

At the same time, in many physical systems, the dissipative effects may be relatively weaker than the dispersive ones, and in such cases, so-called "dispersive shock waves" (DSWs) are formed instead of viscous shocks. DSWs can be represented as modulated nonlinear oscillations whose envelope varies over characteristic distances much greater than their wavelength. In recent years, such systems have attracted much attention in fluid dynamics, nonlinear optics, physics of Bose-Einstein condensates, and other areas of physics (see, e.g., Refs. 3 and 4). This type of problem was studied for the first time in the context of the physics of shallow water waves whose evolution is described by the celebrated Korteweg-de Vries (KdV) equation.[5,6] The equations governing the slow evolution of the envelope of the nonlinear oscillations had been derived by Whitham,[7] and later, they were applied to the description of the DSW structure by Gurevich and Pitaevskii.[8] Because of the universality of the KdV equation, this approach can naturally be applied to many other physical situations. When the condition of unidirectional propagation is relaxed, shallow water waves are described by various forms of Boussinesq equation.[9] The most convenient form for our purpose has been derived by Kaup;[10] this is the so-called Kaup-Boussinesq (KB) equation. The KB equation is completely integrable, and the well-developed methods of inverse scattering transform and finite-gap integration can be used for explicitly deriving its multi-soliton and (quasi-)periodic solutions.[11]

In the applications of this theory to concrete physical problems, only the KB equations with negative dispersion have been considered so far. In this case, linear perturbations can be sought under the form of plane waves with angular frequency ω and wavelength k. In non-dimensional notations, the corresponding dispersion relation reads (h_0 is a constant depth)

$$\omega^2 = h_0 k^2 - \frac{1}{4}k^4. \tag{1}$$

The Whitham modulation equations were derived for this case in Ref. 12, and a complete classification of all the possible wave structures resulting from an initial discontinuous profile was obtained. Besides that, the analytic solution for a generic wave breaking regime was found in Ref. 13—with

the use of a generalized hodograph transform—and stationary undular bore structures whose form was stabilized by weak viscous effects were studied in Ref. 14. However, the dispersion relation (1) corresponds to a dynamical instability of small wavelength perturbations over a fluid of constant depth h_0. There exists another form of the KB system, with positive dispersion, for which the dispersion relation of linear waves reads

$$\omega^2 = h_0 k^2 + \frac{1}{4} k^4. \tag{2}$$

The corresponding KB system can be written under the following non-dimensional form:

$$h_t + (hu)_x - \frac{1}{4} u_{xxx} = 0,$$
$$u_t + uu_x + h_x = 0. \tag{3}$$

In the context of shallow water wave physics, h is the local height of the water layer and u is a local mean flow velocity.[15] Equation (2) represents the dispersion relation of linear waves propagating along a uniform background characterized by the physical variables $h_0 = $ const and $u_0 = 0$. It does not suffer from the instability of Eq. (1). The positive dispersion KB system (3) may be obtained in the case of capillary waves propagating on top of a thin fluid layer (see, e.g., Ref. 3). Besides this physical realization, the system (3) appears as an approximation to the Landau-Lifshitz equation for the propagation of magnetization waves in easy-plane magnets and to the Gross-Pitaevskii equations for the propagation of polarization waves in two-component Bose-Einstein condensates.[16]

Motivated by these applications of the KB system (3), we consider in the present paper the so-called Riemann problem. This corresponds to the study of the time evolution of initial discontinuous profiles of the form

$$h(x, t = 0) = h_L, \quad \text{and} \quad u(x, t = 0) = u_L \text{ for } x < 0,$$
$$h(x, t = 0) = h_R, \quad \text{and} \quad u(x, t = 0) = u_R \text{ for } x > 0. \tag{4}$$

As we shall see, the resulting wave structures differ considerably from those found in Ref. 12 for the negative dispersion case. In the case of Eq. (3) studied in the present work, the classification of the possible wave structures follows closely the scheme found for the nonlinear Schrödinger equation in Refs. 17 and 18. We shall obtain simple analytic formulae for the main parameters of the wave structures and confirm their accuracy by comparison with numerical solutions of the KB system (3).

II. PERIODIC WAVES AND WHITHAM MODULATION EQUATIONS

In this section, we derive the periodic wave solutions (the so-called cnoidal waves) of the system (3) and the Whitham equations governing the modulational dynamics of a cnoidal wave. This is achieved by using the methods described, e.g., in Ref. 3 (see also Ref. 13). These techniques are based on the possibility to represent the system (3) as a compatibility condition for the linear system[10]

$$\psi_{xx} = \mathcal{A}\psi, \quad \psi_t = -\frac{1}{2}\mathcal{B}_x\psi + \mathcal{B}\psi_x \tag{5}$$

with

$$\mathcal{A} = h - \left(\lambda - \frac{1}{2}u\right)^2, \quad \text{and} \quad \mathcal{B} = -\left(\lambda + \frac{1}{2}u\right), \tag{6}$$

where λ is a free spectral parameter. Demanding that $(\psi_{xx})_t = (\psi_t)_{xx}$ for any λ, we reproduce the KB system (3).

The second order spatial linear differential equation in (5) has two independent solutions $\psi_+(x, t)$ and $\psi_-(x, t)$. Their product $g = \psi_+\psi_-$ satisfies the following third order equation:

$$g_{xxx} - 2\mathcal{A}_x g - 4\mathcal{A}g_x = 0. \tag{7}$$

Upon multiplication by g, this equation can be integrated once to give

$$\frac{1}{2}gg_{xx} - \frac{1}{4}g_x^2 - \mathcal{A}g^2 = P(\lambda), \tag{8}$$

where the integration constant has been written as $P(\lambda)$ since it can only depend on λ. The time dependence of $g(x, t)$ is determined by the equation

$$g_t = \mathcal{B}g_x - \mathcal{B}_x g. \tag{9}$$

We are interested in the one-phase periodic solutions of the system (3). They are distinguished by the condition that $P(\lambda)$ in (8) is a fourth degree polynomial of the form[19]

$$P(\lambda) = \prod_{i=1}^{4}(\lambda - \lambda_i) = \lambda^4 - s_1\lambda^3 + s_2\lambda^2 - s_3\lambda + s_4. \tag{10}$$

In expression (10), we chose for definiteness to order the zeroes λ_i according to

$$\lambda_1 \leq \lambda_2 \leq \lambda_3 \leq \lambda_4. \tag{11}$$

Then we find from Eq. (8) that $g(x, t)$ is a first-degree polynomial in λ, of the form

$$g(x, t) = \lambda - \mu(x, t), \tag{12}$$

where $\mu(x, t)$ is connected with $u(x, t)$ and $h(x, t)$ by the relations

$$u(x, t) = s_1 - 2\mu(x, t),$$
$$h(x, t) = \frac{1}{4}s_1^2 - s_2 - 2\mu^2(x, t) + s_1\mu(x, t), \tag{13}$$

which follow from a comparison of the coefficients of the different powers of λ on both sides of Eq. (8). The spectral parameter λ is arbitrary, and on substitution of $\lambda = \mu$ into Eq. (8), we obtain an equation for μ,

$$\mu_x = 2\sqrt{-P(\mu)},$$

while a similar substitution into Eq. (9) gives

$$\mu_t = -\left(\mu + \frac{1}{2}u\right)\mu_x = -\frac{1}{2}s_1\mu_x.$$

Hence, $\mu(x, t)$ and $u(x, t)$ and $h(x, t)$ depend only on the phase

$$\theta = x - \frac{1}{2}s_1 t, \tag{14}$$

so that

$$V = \frac{1}{2}s_1 = \frac{1}{2}\sum_{i=1}^{4}\lambda_i \tag{15}$$

is the phase velocity of the nonlinear wave, and $\mu(\theta)$ is determined by the equation

$$\mu_\theta = 2\sqrt{-P(\mu)}. \tag{16}$$

It follows from Eq. (13) that the variable μ must be real. For the fourth degree polynomial (10), the real solution of (16) corresponds to oscillations of μ in one of the two possible intervals,

$$\lambda_1 \leq \mu \leq \lambda_2 \quad \text{or} \quad \lambda_3 \leq \mu \leq \lambda_4, \tag{17}$$

within which $P(\mu)$ assumes negative values. It is well known that the solution of Eq. (16) with boundaries (17) can be expressed in terms of elliptic functions (see, e.g., Refs. 20 and 21). Without going into details, we shall list here the results which are the most relevant to our study.

• For the case

$$\lambda_1 \leq \mu \leq \lambda_2 \tag{18}$$

the cnoidal wave solution of Eq. (17) with the initial condition $\mu(0) = \lambda_1$ is given by

$$\mu(\theta) = \lambda_2 - \frac{(\lambda_2 - \lambda_1)\mathrm{cn}^2(W, m)}{1 + \dfrac{\lambda_2 - \lambda_1}{\lambda_4 - \lambda_2}\mathrm{sn}^2(W, m)}, \tag{19}$$

where $W = \sqrt{(\lambda_3 - \lambda_1)(\lambda_4 - \lambda_2)}\,\theta$ and

$$m = \frac{(\lambda_2 - \lambda_1)(\lambda_4 - \lambda_3)}{(\lambda_3 - \lambda_1)(\lambda_4 - \lambda_2)} \tag{20}$$

is the modulus of the Jacobi elliptic functions sn and cn. Substitution of (19) into (13) gives the corresponding expressions for $u(\theta)$ and $h(\theta)$ for a one-phase periodic nonlinear wave. Its wavelength is given by

$$L = \int_{\lambda_1}^{\lambda_2} \frac{d\mu}{\sqrt{-P(\mu)}} = \frac{2K(m)}{\sqrt{(\lambda_3 - \lambda_1)(\lambda_4 - \lambda_2)}}, \tag{21}$$

where $K(m)$ is the complete elliptic integral of the first kind. The soliton solution corresponds to the limit $\lambda_3 \to \lambda_2$ ($m \to 1$). We obtain

$$\mu(\theta) = \lambda_2 - \frac{\lambda_2 - \lambda_1}{\cosh^2 W + \dfrac{\lambda_2 - \lambda_1}{\lambda_4 - \lambda_2}\sinh^2 W}. \tag{22}$$

This is a dark soliton solution for the variable μ. In the limit $\lambda_2 \to \lambda_1$, we get a small-amplitude harmonic wave

$$\mu = \lambda_2 - \frac{1}{2}(\lambda_2 - \lambda_1)\cos[k(x - Vt)],$$
$$\text{where} \quad k = 2\sqrt{(\lambda_3 - \lambda_1)(\lambda_4 - \lambda_1)}. \tag{23}$$

If $\lambda_4 = \lambda_3$ but $\lambda_1 \neq \lambda_2$, then we have again $m = 0$ and (22) reduces to a nonlinear trigonometric wave, but we shall not present its explicit form here (cf. e.g., Refs. 20 and 21).

• In a similar way, for the case

$$\lambda_3 \leq \mu \leq \lambda_4, \tag{24}$$

the cnoidal wave solutions are of the form $[\mu(0) = \lambda_4]$

$$\mu(\theta) = \lambda_3 + \frac{(\lambda_4 - \lambda_3)\mathrm{cn}^2(W, m)}{1 + \dfrac{\lambda_4 - \lambda_3}{\lambda_3 - \lambda_1}\mathrm{sn}^2(W, m)}. \tag{25}$$

In the soliton limit $\lambda_3 \to \lambda_2$ ($m \to 1$), we obtain

$$\mu(\theta) = \lambda_2 + \frac{\lambda_4 - \lambda_2}{\cosh^2 W + \dfrac{\lambda_4 - \lambda_2}{\lambda_2 - \lambda_1}\sinh^2 W}. \tag{26}$$

This is a bright soliton (for μ-variable) over a constant background. In the limit $\lambda_4 \to \lambda_3$, we get a small-amplitude harmonic wave

$$\mu = \lambda_3 + \frac{1}{2}(\lambda_4 - \lambda_3)\cos[k(x - Vt)],$$
$$\text{where} \quad k = 2\sqrt{(\lambda_3 - \lambda_1)(\lambda_3 - \lambda_1)}. \tag{27}$$

As discussed above, nonlinear trigonometric waves also exit, here in the case where $\lambda_1 = \lambda_2$ but $\lambda_3 \neq \lambda_4$. If furthermore $\lambda_3 \to \lambda_1$, one reaches the limit of an algebraic soliton[20,21]

$$\mu(\theta) = \lambda_1 + \frac{\lambda_4 - \lambda_1}{1 + (\lambda_4 - \lambda_1)^2\theta^2}. \tag{28}$$

• We now consider slowly modulated cnoidal waves. In this case, the parameters λ_i ($i = 1, 2, 3, 4$) become slowly varying functions of x and t changing weakly over a wavelength L. Their evolution is governed by the Whitham modulation equations[3,4]

$$\frac{\partial \lambda_i}{\partial t} + v_i\frac{\partial \lambda_i}{\partial x} = 0, \quad i = 1, 2, 3, 4. \tag{29}$$

The Whitham velocities v_i appearing in Eq. (29) can be computed *via* the formulae (see, e.g., Refs. 3 and 4)

$$v_i(\lambda_1, \lambda_2, \lambda_3, \lambda_4) = \left(1 - \frac{L}{\partial_{\lambda_i}L}\partial_{\lambda_i}\right)V, \quad i = 1, 2, 3, 4, \tag{30}$$

where the phase velocity V and the wavelength L are given by Eqs. (15) and (21). A simple calculation yields the explicit expressions

$$v_1 = \frac{1}{2}\sum_{i=1}^{4}\lambda_i - \frac{(\lambda_4 - \lambda_1)(\lambda_2 - \lambda_1)K(m)}{(\lambda_4 - \lambda_1)K(m) - (\lambda_4 - \lambda_2)E(m)},$$

$$v_2 = \frac{1}{2}\sum_{i=1}^{4}\lambda_i + \frac{(\lambda_3 - \lambda_2)(\lambda_2 - \lambda_1)K(m)}{(\lambda_3 - \lambda_2)K(m) - (\lambda_3 - \lambda_1)E(m)},$$

$$v_3 = \frac{1}{2}\sum_{i=1}^{4}\lambda_i - \frac{(\lambda_4 - \lambda_3)(\lambda_3 - \lambda_2)K(m)}{(\lambda_3 - \lambda_2)K(m) - (\lambda_4 - \lambda_2)E(m)}, \quad (31)$$

$$v_4 = \frac{1}{2}\sum_{i=1}^{4}\lambda_i + \frac{(\lambda_4 - \lambda_2)(\lambda_4 - \lambda_1)K(m)}{(\lambda_4 - \lambda_1)K(m) - (\lambda_3 - \lambda_1)E(m)},$$

where m is given by (20) and $K(m)$ and $E(m)$ are complete elliptic integrals of the first and second kind, respectively.

In the soliton limit $m \to 1$ (i.e., $\lambda_3 \to \lambda_2$), the Whitham velocities reduce to

$$v_1 = \frac{1}{2}(3\lambda_1 + \lambda_4), \quad v_2 = v_3 = \frac{1}{2}(\lambda_1 + 2\lambda_2 + \lambda_4),$$

$$v_4 = \frac{1}{2}(\lambda_1 + 3\lambda_4). \quad (32)$$

In a similar way, in the small amplitude limit $m \to 0$ (i.e., $\lambda_2 \to \lambda_1$) we obtain

$$v_1 = v_2 = 2\lambda_1 + \frac{(\lambda_4 - \lambda_3)^2}{2(\lambda_3 + \lambda_4 - 2\lambda_1)},$$

$$v_3 = \frac{1}{2}(3\lambda_3 + \lambda_4), \quad v_4 = \frac{1}{2}(\lambda_3 + 3\lambda_4), \quad (33)$$

and in another small amplitude limit ($m \to 0$ when $\lambda_3 \to \lambda_4$) we have

$$v_1 = \frac{1}{2}(3\lambda_1 + \lambda_2), \quad v_2 = \frac{1}{2}(\lambda_1 + 3\lambda_2),$$

$$v_3 = v_4 = 2\lambda_4 + \frac{(\lambda_2 - \lambda_1)^2}{2(\lambda_1 + \lambda_2 - 2\lambda_4)}. \quad (34)$$

III. KEY ELEMENTS OF SELF-SIMILAR WAVE STRUCTURES

The initial profiles (4), being infinitely sharp, do not involve any characteristic length. However the dispersion relation (2) is characterized by the value of the shallow water wave velocity: $c_s = \omega/k|_{k\to 0} = \sqrt{h_0}$. Therefore, the large scale features of the solution of this problem (with characteristic length scale much greater than the wavelength) can only depend on the self-similar variable $\xi = x/t$, which can be made non-dimensional with the help of the velocity c_s. This means that the large scale features of the wave pattern must be self-similar and should be composed of (possibly several) regions where h and v either smoothly depend on ξ, or consist of modulated periodic waves whose envelopes (and wavelength L) depend slowly on ξ.

In the framework of the hydrodynamic approximation, these regions are separated by weak discontinuities where the physical variables have cusps. If the hydrodynamic approximation leads to non-monotonous dependence of velocities on the wave amplitude, then the wave structure

can be more complicated; an example of such a situation was considered, e.g., in Ref. 20. At first we shall consider smooth solutions of the KB system (3).

A. Dispersionless limit

For smooth enough wave patterns, we can neglect the last dispersive term in the first equation of the system (3) and arrive at the so-called dispersionless equations

$$h_t + (hu)_x = 0, \quad u_t + uu_x + h_x = 0, \quad (35)$$

which coincide with the well-known shallow water equations. Introducing the Riemann invariants

$$\lambda_\pm = \frac{u}{2} \pm \sqrt{h}, \quad (36)$$

the system (35) can be written in the following diagonal form:

$$\frac{\partial \lambda_\pm}{\partial t} + v_\pm(\lambda_-, \lambda_+)\frac{\partial \lambda_\pm}{\partial x} = 0,$$

$$\text{where} \quad v_\pm(\lambda_-, \lambda_+) = \frac{1}{2}(3\lambda_\pm + \lambda_\mp). \quad (37)$$

The physical variables are expressed in terms of $\lambda_\pm$ as

$$u = \lambda_+ + \lambda_-, \quad h = (\lambda_+ - \lambda_-)^2/4. \quad (38)$$

For the self-similar solutions, one has $\lambda_\pm = \lambda_\pm(\xi)$ and the system (37) reduces to

$$\frac{d\lambda_+}{d\xi} \cdot (v_+ - \xi) = 0, \quad \frac{d\lambda_-}{d\xi} \cdot (v_- - \xi) = 0. \quad (39)$$

This system admits a trivial solution for which $\lambda_+ = \text{const}$ and $\lambda_- = \text{const}$. It describes a uniform flow with constants h and u. We shall call such a solution a "plateau."

Other solutions of (39) are called simple waves. For such flows, one of the Riemann invariants is constant (say, λ_-), whereas the other one changes in such a way that the term between parenthesis in its equation is zero ($v_+ = \xi$ in the example considered). One has thus two possible types of self-similar simple waves:

$$\begin{cases} \lambda_- = C^{st} \equiv \bar{\lambda}_-, \quad \text{with} \\ v_+(\bar{\lambda}_-, \lambda_+) = \frac{1}{2}(3\lambda_+ + \bar{\lambda}_-) = \xi = x/t, \end{cases} \quad (40)$$

or

$$\begin{cases} \lambda_+ = C^{st} \equiv \bar{\lambda}_+, \quad \text{with} \\ v_-(\lambda_-, \bar{\lambda}_+) = \frac{1}{2}(3\lambda_- + \bar{\lambda}_+) = \xi = x/t. \end{cases} \quad (41)$$

The constancy of one of the Riemann invariants means that h and u are related by a simple formula: either $\lambda_- = u/2 - h^{1/2} = \text{const} = \bar{\lambda}_- = \bar{u}/2 - \bar{h}^{1/2}$ or $\lambda_+ = u/2 + h^{1/2} = \text{const} = \bar{\lambda}_+ = \bar{u}/2 + \bar{h}^{1/2}$, where $\bar{u}$ and $\bar{h}$ are some values that fix the value of the constant Riemann invariant and can be chosen at convenience for solving a specific problem.

Thus, for given values of $\bar{u}$ and $\bar{h}$, a simple wave corresponds to a configuration where the variables u and h are connected by the relations corresponding to one of the two parabolae drawn in the plane (u, h) in Fig. 1. The parabolae cross at the point $P = (\bar{u}, \bar{h})$, which represents a uniform flow with constant values of $u = \bar{u}$ and $h = \bar{h}$ which is a trivial "plateau solution" of Eq. (35).

The dispersionless system (35) requires continuity of the functions $u(x, t)$ and $h(x, t)$, but, as usual in hydrodynamics, admits jumps of their space derivatives, i.e., "weak discontinuities." Therefore, a plateau solution $(\bar{u}, \bar{h})$ can be attached at one of its boundaries to a simple wave. We have here two possibilities. If the uniform flow corresponding to $P = (\bar{u}, \bar{h})$ matches with the simple wave along which $\lambda_+ = \bar{\lambda}_+ = \text{const}$ (one of the solid parabolae in Fig. 1), then from Eq. (41) one gets for this flow

$$\begin{cases} u(x,t) = \dfrac{2}{3}\left(\dfrac{x}{t} + \bar{\lambda}_+\right) = \dfrac{2}{3}\left(\dfrac{x}{t} + \dfrac{\bar{u}}{2} + \sqrt{\bar{h}}\right), \\ h(x,t) = \dfrac{1}{9}\left(\dfrac{x}{t} - 2\bar{\lambda}_+\right) = \dfrac{1}{9}\left(\dfrac{x}{t} - \bar{u} - 2\sqrt{\bar{h}}\right)^2. \end{cases} \quad (42)$$

This wave configuration represents a rarefaction wave (RW) propagating to the right. If it propagates into "vacuum," then Eq. (42) gives the full solution of the problem (4) with left boundaries $h_L = \bar{h}$ and $u_L = \bar{u}$, whereas at the right boundary $h_R = 0$ (the value of u_R is irrelevant in the space without fluid). This situation is depicted in Fig. 2(a). The left edge of this rarefaction wave propagates to the left at the velocity $s_- = u_L - \sqrt{h_L}$ and the right edge propagates to the right into the empty space with the velocity $s_+ = u_L + 2\sqrt{h_L}$.

In a similar way, if $P = (\bar{u}, \bar{h})$ matches with the simple wave along which $\lambda_- = \bar{\lambda}_- = \text{const}$, then (40) yields

$$\begin{cases} u(x,t) = \dfrac{2}{3}\left(\dfrac{x}{t} + \bar{\lambda}_-\right) = \dfrac{2}{3}\left(\dfrac{x}{t} + \dfrac{\bar{u}}{2} + \sqrt{\bar{h}}\right), \\ h(x,t) = \dfrac{1}{9}\left(\dfrac{x}{t} - 2\bar{\lambda}_-\right) = \dfrac{1}{9}\left(\dfrac{x}{t} - \bar{u} + 2\sqrt{\bar{h}}\right)^2. \end{cases} \quad (43)$$
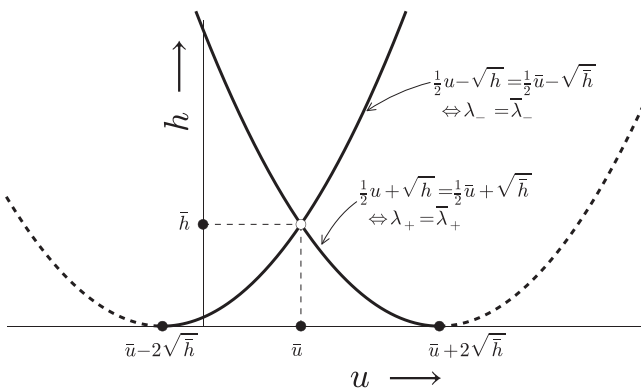

FIG. 1. Relation between u and h for simple wave solutions in the dispersionless regime. The solid lines correspond to the curve $\lambda_+ = C^{\text{st}} = \bar{\lambda}_+$ [portion of parabola ending at point with coordinates $(\bar{u} + 2\sqrt{\bar{h}}, 0)$] and to the curve $\lambda_- = C^{\text{st}} = \bar{\lambda}_-$ [portion of parabola ending at point $(\bar{u} - 2\sqrt{\bar{h}}, 0)$]. They are continued by the dashed curves along which $\lambda_- = \bar{\lambda}_+$ (right dashed curve) and $\lambda_+ = \bar{\lambda}_-$ (left dashed curve). These dashed curves are of no significance for the present discussion of simple waves, but will become important in Sec. IV.
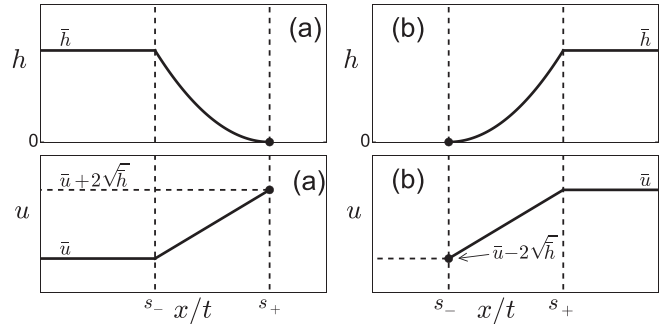

FIG. 2. Height and velocity profiles for self-similar rarefaction wave solutions of the dispersionless equations (35) expanding into empty space (the so-called "dam problem"). Panel (a) corresponds to a flow expanding in the positive x direction and panel (b) to a flow expanding in the negative x direction. The values of the edge velocities $s_\pm$ are given in the text.

This represents a rarefaction wave propagating to the left. Again, it corresponds—in the hydrodynamic approximation—to the solution of the problem (4) with $h_L = 0$, whereas at the right boundary $h_R = \bar{h}$ and $u_R = \bar{u}$ (see Fig. 2(b)). The edge velocities are equal to $s_- = u_R - 2\sqrt{h_R}$ and $s_+ = u_R + \sqrt{h_R}$.

It is clear that we can generalize these solutions to the cases where both sides of the rarefaction wave connect uniform flows with equal values of the corresponding Riemann invariants $u_L/2 + \sqrt{h_L} = u_R/2 + \sqrt{h_R}$ or $u_L/2 - \sqrt{h_L} = u_R/2 - \sqrt{h_R}$. In these cases, the rarefaction wave connects two uniform flows and the corresponding distributions of h and u are shown in Fig. 3. The velocities of the edges of the rarefaction waves are given in both cases by the formulae $s_- = u_L - \sqrt{h_L}$, $s_+ = u_R + \sqrt{h_R}$. These values have simple physical interpretation: they are the sums of the local flow velocities (u_L or u_R) and of the propagation velocities of small amplitude disturbances directed to the left for the left edge ($-\sqrt{h_L}$) and to the right for the right edge ($+\sqrt{h_R}$).

It is important to note that the system (39) only admits solutions of the type (40) and (41) for which the non-constant Riemann invariant increases with $\xi = x/t$. The above wave structures correspond to the conditions (a) $\lambda_+^L < \lambda_+^R$, $\lambda_-^L = \lambda_-^R$ or (b) $\lambda_+^L = \lambda_+^R$, $\lambda_-^L < \lambda_-^R$, as illustrated in Figs. 4(a) and 4(b). The other two situations represented in Figs. 4(c) and 4(d), that is (c) $\lambda_+^L = \lambda_+^R$, $\lambda_-^L > \lambda_-^R$ and (d) $\lambda_+^L > \lambda_+^R$, $\lambda_-^L = \lambda_-^R$, result in multi-valued solutions and are
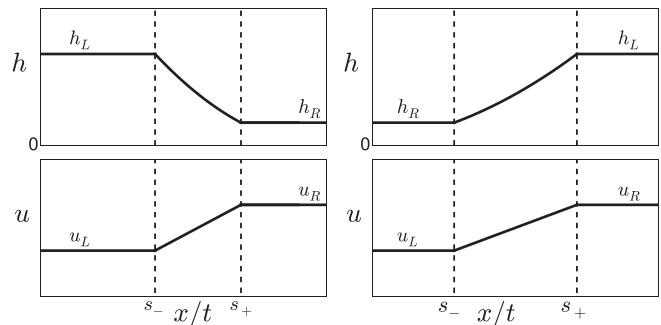

FIG. 3. Self-similar solutions of the dispersionless equations (35) composed by a rarefaction wave connecting two uniform flows. The two left plots correspond to the situation where $\lambda_+ = \text{const}$ for the whole flow; the two right ones to $\lambda_- = \text{const}$.
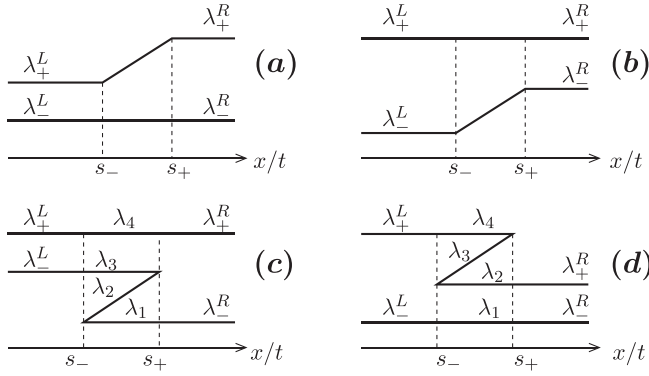
FIG. 4. Diagrams representing the evolution of the Riemann invariants as a function of x/t. Plots (a) and (b) correspond to the configuration where a dispersionless rarefaction wave connects two uniform flows. Plots (c) and (b) considered within the dispersionless approximation correspond to a formal multi-valued solution. In this case, the dispersionless approximation breaks down and one observes a dispersive shock wave, accurately described by 4 Riemann invariants within the Whitham modulational approach, cf. Sec. III B.

therefore nonphysical: the dispersionless approximation is not applicable in these cases and we have to turn to another type of key elements for describing such structures.

B. Dispersive shock waves

Since the pioneering work of Gurevich and Pitaevskii,[8] it is known that wave breaking—such as depicted in Figs. 4(c) and 4(d) for the dispersionless Riemann invariants—is regularized by the replacement of the nonphysical multi-valued dispersionless solution by a dispersive shock wave. This wave pattern can be represented approximately as a modulated nonlinear periodic wave whose parameters λ_i ($i = 1, 2, 3, 4$, cf. Sec. II) change slowly along the wave structure. In this case, the two dispersionless Riemann invariants $\lambda_\pm$ are replaced in the DSW region by four Riemann invariants λ_i (cf. Figs. 4(c) and 4(d)). In this region, the evolution of the DSW is determined by the Whitham equations (29). In our case, when we consider of self-similar solution, all Riemann invariants depend only on $\xi = x/t$, and the Whitham equations reduce to

$$\frac{d\lambda_i}{d\xi} \cdot [v_i(\lambda_1, \lambda_2, \lambda_3, \lambda_4) - \xi] = 0, \quad i = 1, 2, 3, 4. \quad (44)$$

One of the two factors in this equation must vanish, that is, for each i, either the Riemann invariant λ_i is constant, or $v_i = \xi$. For the Whitham velocities (31), there exist solutions for which, in the DSW region, only one of the Riemann invariants varies, whereas the three others remain constant. These solutions correspond qualitatively to the same patterns as the ones depicted in Figs. 4(c) and 4(d). However, naturally, the dependence of the Riemann invariants on ξ resulting from (44) differs from the one obtained from (39) (different equations and different variables). As a result, the velocities of the edges of the DSW do not coincide with the velocities of the nonphysical solutions of the dispersionless equations. It nonetheless remains true that Figs. 4(c) and 4(d) schematically represent the structure of the Riemann invariants for the solutions of the Whitham equations (44):

in Fig. 4(c), λ_2 varies and (λ_1, λ_3, λ_4) remain constant, whereas in Fig. 4(d), λ_3 varies and (λ_1, λ_2, λ_4) remain constant. We thus arrive at the following description of these solutions:

- In the case of Fig. 4(c) where $\lambda_+^L = \lambda_+^R$, $\lambda_-^L > \lambda_-^R$ we have

$$\lambda_1 = \lambda_-^R, \quad \lambda_3 = \lambda_-^L, \quad \lambda_4 = \lambda_+^L = \lambda_+^R, \quad (45)$$

and λ_2 depends on ξ according to the equation

$$v_2(\lambda_-^R, \lambda_2, \lambda_-^L, \lambda_+^L) = \xi. \quad (46)$$

The resulting wave pattern is obtained by substitution of these values of (λ_1, λ_2, λ_3, λ_4) into (19) and (13). The left, small amplitude, edge of the DSW propagates with the velocity

$$s_- = 2\lambda_+^R + \frac{\left(\lambda_+^L - \lambda_-^L\right)^2}{2\left(\lambda_+^L + \lambda_-^L - 2\lambda_+^R\right)}. \quad (47)$$

The right edge corresponds to the soliton limit, propagating with the velocity

$$s_+ = \frac{1}{2}\left(\lambda_-^R + 2\lambda_-^L + \lambda_+^L\right). \quad (48)$$

- In a similar way, in the case of Fig. 4(d) where $\lambda_+^L > \lambda_+^R$, $\lambda_-^L = \lambda_-^R$ we have

$$\lambda_1 = \lambda_-^L = \lambda_-^R, \quad \lambda_2 = \lambda_+^R, \quad \lambda_4 = \lambda_+^L, \quad (49)$$

and the dependence of λ_3 on ξ is determined by the implicit equation

$$v_3(\lambda_-^R, \lambda_+^R, \lambda_3, \lambda_+^L) = \xi. \quad (50)$$

Substitution of the values of λ_i resulting from (49) and (50) into (25) and then (13) yields the oscillatory DSW structure for the physical variables u and h. The left edge of the DSW corresponds to the soliton limit and this soliton moves with the velocity

$$s_- = \frac{1}{2}\left(\lambda_-^R + 2\lambda_+^R + \lambda_+^L\right). \quad (51)$$

Its right edge corresponds to the small amplitude limit propagating with the velocity

$$s_+ = 2\lambda_+^L + \frac{\left(\lambda_+^R - \lambda_-^L\right)^2}{2\left(\lambda_+^R + \lambda_-^R - 2\lambda_+^L\right)}. \quad (52)$$

IV. CLASSIFICATION OF SOLUTIONS OF THE RIEMANN PROBLEM

For a given choice of initial conditions (4), the solution of the Riemann problem consists of combinations of the key elements listed in the preceding Sec. III: plateaus, rarefaction waves and dispersive shocks. It is important to notice that if

an RW or a DSW matches with a plateau at its both left and right edges, then these plateaus share one of their (dispersionless) Riemann invariants. For example, in Figs. 4(a) and 4(d), we have $\lambda_-^L = \lambda_-^R$ and in Figs. 4(b) and 4(c) we have $\lambda_+^L = \lambda_+^R$.

Also, in the case of a DSW, despite the fact that the dynamics inside the shock region is described by four Riemann invariants, two of them coincide with the dispersionless invariants of one of the plateaus at the edges of the shock. Hence one may say that the value of one of the dispersionless Riemann invariants [λ_- say, as in the case of Fig. 4(d)] is "transferred" through the DSW, although, if it were computed using formula (36), one would find that it strongly oscillates inside the DSW region. The equality $\lambda_-^L = \lambda_-^R$ [for the case of Fig. 4(d)] connects the parameters of the flow at both sides of the dispersive shock, and in this sense, it plays a role similar to that of the Rankine-Hugoniot condition in the theory of viscous shocks (see Refs. 22 and 23).

Due to this property of the dispersionless Riemann invariants, the points corresponding to the edges of the DSW (or of the RW) must lie on one of the parabolae along which the value of the dispersionless Riemann invariant remains constant. Hence, the dispersionless parabolae of Fig. 1 are useful tools for the classification of all possible solutions. One should keep in mind that the parabolic arcs symbolize the different types of solutions: a physically acceptable single-valued RW [Figs. 4(a) and 4(b)] or a formal multi-valued solution [Figs. 4(c) and 4(d)] which should be replaced by a DSW correctly treated within the Whitham approach. After these preliminary remarks, we can proceed to the classification of the wave structures.

The left and right boundaries of the whole wave structure connect with undisturbed plateau regions whose parameters coincide with the initial conditions (4); for instance, in any situation, one should always have at the left boundary: $u(x/t \le s_-^L) = u_L$ and $h(x/t \le s_-^L) = h_L$. Consequently, the left and right edges propagate into plateau regions represented by the two points (u_L, h_L) and (u_R, h_R) in the (u, h) plane. We represent in Fig. 5 the two parabolae corresponding to the constant dispersionless invariants $\lambda_\pm^L = u_L/2 \pm \sqrt{h_L}$ including their branches extending beyond the tangent points with the u-axis (which were represented as dashes lines in Fig. 1). These parabolae cut the physical half-plane $h > 0$ into six domains labeled by the symbols $A, B, \ldots, F$.
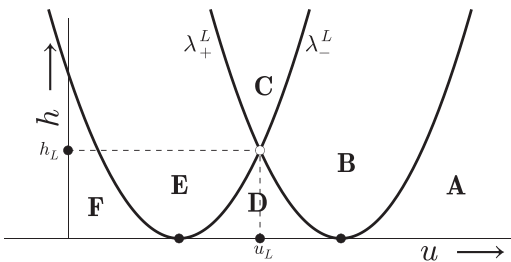

FIG. 5. Regions in the (u, h) plane corresponding to different types of flow. The left boundary corresponds to point L of coordinates (u_L, h_L). The two parabolae are defined by the equations $h = (\frac{1}{2}u - \lambda_+^L)^2$ and $h = (\frac{1}{2}u - \lambda_-^L)^2$. The type of flow depends on the region (A, B,..., or F) in which lies the right boundary point R of coordinates (u_R, h_R).

Depending on the domain in which the point R with coordinates (u_R, h_R) lies, one has one of the six following possible orderings of the left and right Riemann invariants:

$$
\begin{array}{ll}
A : \lambda_-^L < \lambda_+^L < \lambda_-^R < \lambda_+^R, & B : \lambda_-^L < \lambda_-^R < \lambda_+^L < \lambda_+^R, \\
C : \lambda_-^R < \lambda_-^L < \lambda_+^L < \lambda_+^R, & D : \lambda_-^L < \lambda_-^R < \lambda_+^R < \lambda_+^L, \\
E : \lambda_-^R < \lambda_-^L < \lambda_+^R < \lambda_+^L, & F : \lambda_-^R < \lambda_+^R < \lambda_-^L < \lambda_+^L.
\end{array}
\tag{53}
$$

These six situations correspond to the six possible wave structures resulting from the initial discontinuous profiles (4). We shall now describe their main properties and parameters. Note that, as expected, the typology below does not depend on the absolute values of u_R and u_L, but only on their relative positions.

(A) In this case, the two rarefaction waves represented in Figs. 2(a) and 2(b) are combined into a single wave structure where they are separated by an empty region [in which $h(x, t) = 0$]. The velocities of the edges of the RWs are given by the formulae

$$
\begin{aligned}
s_-^L &= u_L - \sqrt{h_L}, \quad s_+^L = u_L + 2\sqrt{h_L}, \\
s_-^R &= u_R - 2\sqrt{h_R}, \quad s_+^R = u_R + \sqrt{h_R}.
\end{aligned}
\tag{54}
$$

The corresponding wave structure is displayed in Fig. 6(A). As expected, the dispersionless approximation gives a very accurate description of the solution.

In the hydrodynamic context, this situation corresponds to launching two fluids in opposite directions with velocities so large that the rarefaction waves are not able to fill the empty regions between them.

(B) Here the parabolae $u/2 + \sqrt{h} = u_L/2 + \sqrt{h_L}$ and $u/2 - \sqrt{h} = u_R/2 - \sqrt{h_R}$ cross at the point $P = (u_P, h_P)$ with the Riemann invariants $\lambda_\pm^P = u_P/2 \pm \sqrt{h_P}$, and their equality yields the values of the physical variables

$$
u_P = \lambda_+^P + \lambda_-^P = \frac{1}{2}(u_L + u_R) + \sqrt{h_L} - \sqrt{h_R},
$$

$$
h_P = \frac{1}{4}\left(\lambda_+^P - \lambda_-^P\right)^2 = \frac{1}{4}\left[\frac{1}{2}(u_L - u_R) + \sqrt{h_L} + \sqrt{h_R}\right]^2.
\tag{55}
$$

In this case, one has two rarefaction waves separated by a plateau region, which is represented by point P in the (u, h) plane of Fig. 6(B). The velocities of the edges can be easily found from the self-similar solutions (40) and (41)

$$
\begin{aligned}
s_-^L &= v_-\left(\lambda_-^L, \lambda_+^L\right) = \frac{1}{2}\left(3\lambda_-^L + \lambda_+^L\right) = u_L - \sqrt{h_L}, \\
s_+^L &= v_-\left(\lambda_-^P, \lambda_+^L\right) = \frac{1}{2}\left(3\lambda_-^R + \lambda_+^L\right), \\
s_-^R &= v_+\left(\lambda_-^P, \lambda_+^P\right) = \frac{1}{2}\left(\lambda_-^R + 3\lambda_+^L\right), \\
s_+^R &= v_+\left(\lambda_-^R, \lambda_+^R\right) = \frac{1}{2}\left(\lambda_-^R + 3\lambda_+^R\right) = u_R + \sqrt{h_R}.
\end{aligned}
\tag{56}
$$

The corresponding wave structure is displayed in Fig. 6(B). As in case (A), the dispersionless approximation gives a very accurate description of the solution.
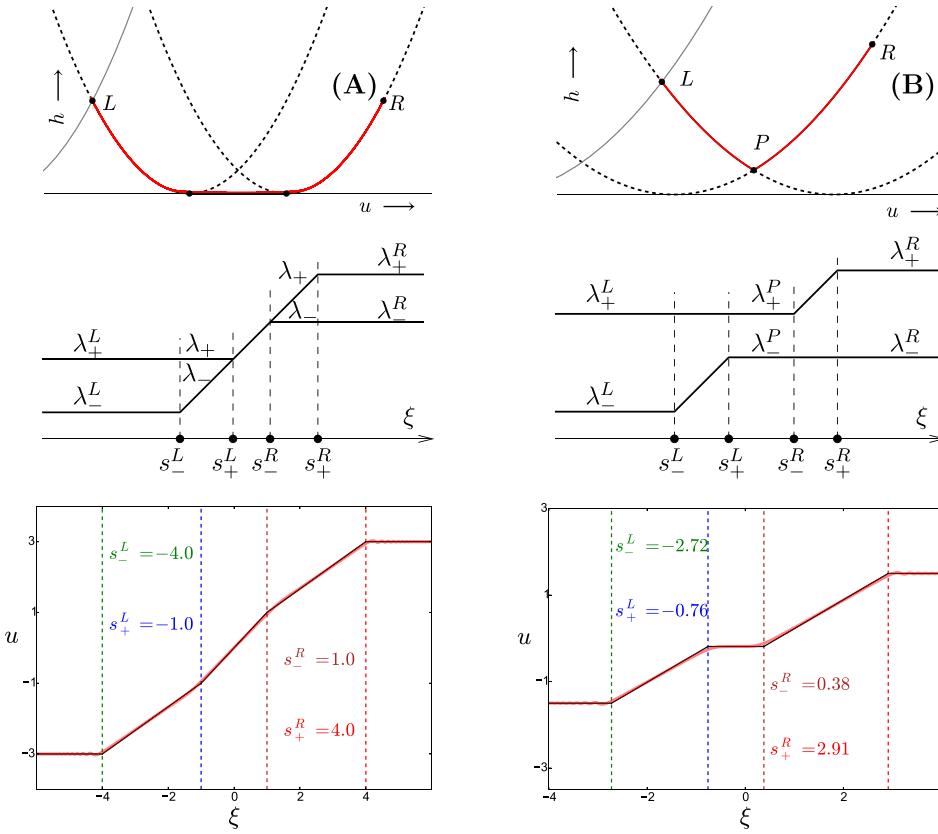
FIG. 6. Solutions in the cases (A) (three plots of the left column) and (B) (three plots of the right column). The initial profiles are characterized by $h_L = 1$, $u_L = -3$, $h_R = 1$, $u_R = 3$ in case (A) and $h_L = 1.5$, $u_L = -1.5$, $h_R = 2$, $u_R = 1.5$ in case (B). The upper plots display the behavior of the solution in the (u, h) plane. The black solid line (almost perfectly recovered by the red line) is the result expected form the dispersionless approximation. The red solid line displays the results of numerical simulations. The middle plots schematically represent the behavior of the Riemann invariant as functions of ξ. These are sketches, not on scale with the two other rows. The lower plots compare the numerical simulations for the velocity field $u(\xi)$ (pink thick lines) with the analytic approach (black solid lines) from the dispersionless approximation. In these plots, the vertical colored line are the velocities of the edges between the different components of the wave structure, as determined from (54) in case (A) and (56) in case (B).

Here the hydrodynamic interpretation is that the two fluids are moving away from each other with velocities lower than in the previous case (A), and the rarefaction waves are now able to provide enough flux of fluid to create a plateau in the region which separates them. This plateau has a fixed value of the height h and the flow velocity u.

(C) In this case, the initial profile evolves to form a DSW on the left, an RW on the right, and a plateau in between. The Riemann invariants in the plateau region are $\lambda_-^P = \lambda_-^R$ and $\lambda_+^P = \lambda_+^L$. In the DSW region, the Riemann invariants behave as schematically represented in Fig. 4(c). The edges of the DSW propagate with velocities

$$s_-^L = v_2\left(\lambda_-^R, \lambda_-^R, \lambda_-^L, \lambda_+^L\right) = 2\lambda_-^R + \frac{\left(\lambda_+^L - \lambda_-^L\right)^2}{2\left(\lambda_+^L + \lambda_-^L - 2\lambda_-^R\right)},$$

$$s_+^L = v_2\left(\lambda_-^R, \lambda_-^L, \lambda_-^L, \lambda_+^L\right) = \frac{1}{2}\left(\lambda_-^R + 2\lambda_-^L + \lambda_+^L\right),$$

(57)

and the velocities of the edges of the RW are equal to

$$s_-^R = v_+\left(\lambda_-^P, \lambda_+^P\right) = \frac{1}{2}\left(\lambda_-^R + 3\lambda_+^L\right),$$

$$s_+^R = v_+\left(\lambda_-^R, \lambda_+^R\right) = \frac{1}{2}\left(\lambda_-^R + 3\lambda_+^R\right).$$

(58)

This situation could be interpreted as if one fluid was colliding with the other flowing away with such velocity that a plateau with increased density is formed between them. The corresponding wave structure is displayed in Fig. 7(C). The right RW and the plateau region are correctly described by

the dispersionless approximation, as can be check on the upper plot of this figure where the two approaches perfectly match between points P (plateau region) and R (right boundary). Of course, this is not true for the DSW: at variance with the behavior expected on the basis of the dispersionless approximation (black solid line), the numerical results (red solid line) display large oscillations between points P and L. This behavior is, however, quite successfully described by the Whitham approach, as can be seen in the lower plot of Fig. 7(C).

(D) Here we have an RW on the left and a DSW on the right with a plateau in between. The Riemann invariants in the plateau region are equal again to $\lambda_-^P = \lambda_-^R$, $\lambda_+^P = \lambda_+^L$. The velocities of the RW's edges are equal to

$$s_-^L = v_-\left(\lambda_-^L, \lambda_+^L\right) = \frac{1}{2}\left(3\lambda_-^L + \lambda_+^L\right),$$

$$s_+^L = v_-\left(\lambda_-^R, \lambda_+^L\right) = \frac{1}{2}\left(3\lambda_-^R + \lambda_+^L\right).$$

(59)

The behavior of the two dispersionless Riemann invariants in the region of the rarefaction wave corresponds to the case illustrated in Fig. 4(b). In the DSW region, there are four Riemann invariants, which behave as schematically represented in Fig. 4(d), and the edges of the DSW propagate with velocities

$$s_-^R = v_3\left(\lambda_-^R, \lambda_+^R, \lambda_+^R, \lambda_+^L\right) = \frac{1}{2}\left(\lambda_-^R + 2\lambda_+^R + \lambda_+^L\right),$$

$$s_+^R = v_3\left(\lambda_-^R, \lambda_+^R, \lambda_+^L, \lambda_+^L\right) = 2\lambda_+^L + \frac{\left(\lambda_+^R - \lambda_-^R\right)^2}{2\left(\lambda_+^R + \lambda_-^R - 2\lambda_+^L\right)}.$$
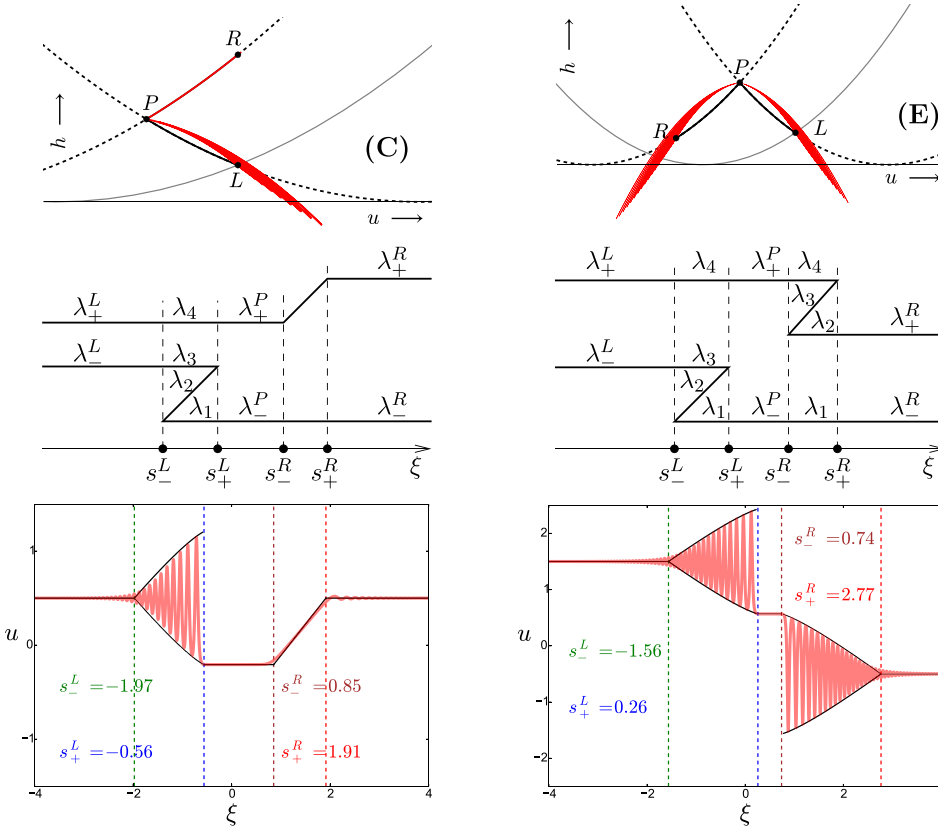
(60)

FIG. 7. Same as Fig. 6 for the cases (C) (three plots of the left column) and (E) (three plots of the right column). The initial profiles are characterized by $h_L = 0.5$, $u_L = 0.5$, $h_R = 2$, $u_R = 0.5$ in case (C) and $h_L = 0.6$, $u_L = 1.5$, $h_R = 0.5$, $u_R = -0.5$ in case (E). The lower plots compares the numerical simulations for the velocity field $u(\xi)$ (pink thick lines) with the theoretical approach (black solid lines) composed of dispersionless approaches (in the plateau and the RW region) and Whitham modulation theory for the DSW. In the region of the DSW, we only display the envelope of the non-linear modulated wave. A more accurate comparison is done in Fig. 8.

This situation is similar to the preceding one upon exchanging the roles of the left and right fluids; we thus do not illustrate it by a figure.

(E) In this case, the initial profile evolves in two DSWs separated by a plateau, the parameters of which are $\lambda_-^P = \lambda_-^R$ and $\lambda_+^P = \lambda_+^L$. The DSW's edges propagate with velocities

$$s_-^L = v_2\left(\lambda_-^R, \lambda_-^R, \lambda_-^L, \lambda_+^L\right) = 2\lambda_-^R + \frac{\left(\lambda_+^L - \lambda_-^L\right)^2}{2\left(\lambda_+^L + \lambda_-^L - 2\lambda_-^R\right)},$$

$$s_+^L = v_2\left(\lambda_-^R, \lambda_-^L, \lambda_-^L, \lambda_+^L\right) = \frac{1}{2}\left(\lambda_-^R + 2\lambda_-^L + \lambda_+^L\right),$$

$$s_-^R = v_3\left(\lambda_-^R, \lambda_+^R, \lambda_+^R, \lambda_+^L\right) = \frac{1}{2}\left(\lambda_-^R + 2\lambda_+^R + \lambda_+^L\right),$$

$$s_+^R = v_3\left(\lambda_-^R, \lambda_+^R, \lambda_+^L, \lambda_+^L\right) = 2\lambda_+^L + \frac{\left(\lambda_+^R - \lambda_-^R\right)^2}{2\left(\lambda_+^R + \lambda_-^R - 2\lambda_+^L\right)}.$$

(61)

Here we have a collision of two fluids with "moderate" velocities: the two DSWs do not overlap, but a central plateau region of increased height is formed. This situation is represented in Fig. 7(E). Again, the theoretical approach quite accurately describes the numerical results (cf. the bottom row).

The upper part of the figure illustrates a phenomenon already present in case (C): the large nonlinear oscillations in the DSW regions are associated with locally negative values of $h(x, t)$. This phenomenon is clearly seen in Fig. 8, which represents h as a function of ξ for the two configurations (C) and (E) considered in Fig. 7. Although extended

regions of constant and negative values of h lead to a dynamical instability [as clearly seen from the dispersion relation (2)], nothing forbids local excursions of h below 0, and this is confirmed by the excellent agreement of the numerical and theoretical results presented in Fig. 8. Of course, in this case, the interpretation of h as being the height of a fluid surface becomes meaningless, but, as explained in the introduction, the physical model behind the nonlinear equations (3) can have an origin different from shallow water physics.

(F) In this configuration, the two fluids collide with velocities so large that the central plateau observed in case (E) disappears: the DSWs overlap and, on the basis of a similar situation observed for the nonlinear Schrödinger equation[18] and for the Landau-Lifshitz equation,[16] one would
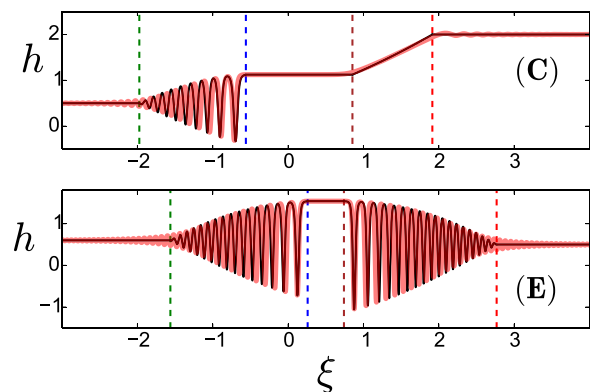

FIG. 8. h as a function of ξ for the same configurations as the ones depicted in Figs. 7(C) and 7(E). The pink solid line represents the results of the numerical simulations, and the black solid line is the theoretical result. Note the numerous excursions of $h(x, t)$ below zero.

expect that the plateau is replaced by a new structure, separating two partial DSWs, which can be approximated by a non-modulated cnoidal wave (whose four Riemann invariants are constant) or more accurately by a two-phase nonlinear wave.

Our numerical simulations show that this is not the case: the collision of the DSW is here associated with a numerical instability which we attribute to a physical dynamical instability of the region of the overlapping DSWs.

V. DAM BREAK AND PISTON PROBLEM

In view of the particularities noticed in Sec. IV—possible negative values of h and dynamical instabilities—it is interesting to study in more detail two model cases, illustrating the specificity of the Kaup-Boussinesq system. The first one is the dam break problem, which corresponds to a particular case of initial conditions (4). The second case is the piston problem. It does not pertain to the same class of initial conditions, but nevertheless provides an instructive insight on non-modulated cnoidal waves whose stability is questioned by the results obtained in case (F).

A. Dam break problem

This is the case where a semi-infinite constant height of water expands into empty space, which would be a model of flow after the abrupt breaking of a dam. Such a configuration is schematically described by an initial condition of type (4) with

$$h_R = 0 \quad \text{and} \quad u_R = 0. \tag{62}$$

On the basis of physical intuition, one expects that the time evolution of this initial profile will result in a rarefaction wave expanding into vacuum, as for the case illustrated in Fig. 2(a). This is not quite correct: such a situation is only reached when u_L is sufficiently negative. More specifically, the initial condition (62) pertains either to case (A) when $u_L < -2\sqrt{h_L}$, to case (D) when $|u_L| < 2\sqrt{h_L}$, or to case (F) when $u_L > 2\sqrt{h_L}$. In other words, this is only when the initial left velocity (the initial velocity of the water of the dam) is negative enough that a rarefaction wave is observed. This behavior is different from the one observed in the similar case for the nonlinear Schrödinger equation.[18] In the present case, the most natural situation where $u_L = 0$ (the water in the dam is initially steady) pertains to case (D) for which the dam break leads to a DSW where the field h becomes negative. Only when u_L becomes negative enough [in practice, when it becomes lower than $-2\sqrt{h_L}$, i.e., when one reaches the regime (A)] does the excursion of $h(x, t)$ below zero disappear.

This point deserves a slightly more detailed discussion: for the dam break problem in case (D), one can easily check that the plateau region has a vanishing extension ($s_+^L = \frac{1}{2}\lambda_+^L = s^R$). The behavior of the Riemann invariants is depicted in Fig. 9. In this case, $\lambda_1 = \lambda_2$ and the DSW is described by a nonlinear trigonometric wave[20,21] whose large amplitude boundary (at s^R) corresponds to an algebraic soliton of type (28) for which the largest value of μ is $\lambda_4 = \lambda_+^L$. Then,
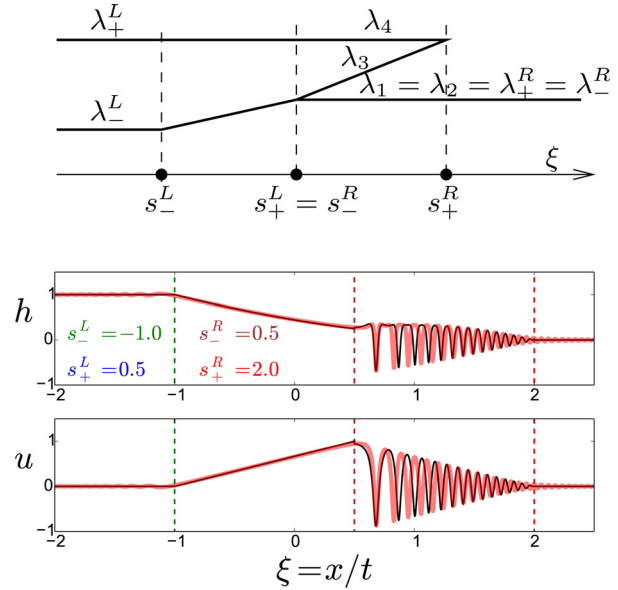

FIG. 9. The upper plot is a sketch of the behavior of the Riemann invariants describing the dam break problem when $|u_L| < 2\sqrt{h_L}$ [type (D) configuration]. The dispersionless Riemann invariants describing the boundary conditions at the right are $\lambda_+^R = \lambda_-^R = 0$, and at the left, $\lambda_\pm^L = \frac{1}{2}u_L \pm \sqrt{h_L}$. The two lower plots compare the results of the numerical simulations (pink solid lines) with the theoretical results (black solid lines) for the boundary condition $h_L = 1$ and $u_L = 0$.

from (13), the corresponding extremal value of h is $-\frac{1}{2}\lambda_4^2 = -\frac{1}{2}(\frac{1}{2}u_L + \sqrt{h_L})^2$: it is always negative, and only vanishes when one leaves regime (D) to enter regime (A), i.e., when $u_L \leq -2\sqrt{h_L}$: in this case, the plateau P and the right boundary R coincide and the flow is of the type exemplified in Fig. 2(a), which corresponds to an RW expanding into empty space, as intuitively expected.

B. Piston problem

The piston problem corresponds to the situation where a hard wall (the piston) is moving (in the case considered here, with a constant positive velocity V) with respect to a steady fluid. We work henceforth in the rest frame of the piston. In this frame, the piston is located at $x = 0$, and the fluid is incoming from the right with a constant velocity $u_R = -V$ and a fixed constant depth h_R. The boundary condition on the piston is $u(0, t) = 0$: the fluid in contact with the piston is at rest with respect to it. The boundary condition for the height is taken as $h(0, t) = 0$, or $h_x(0, t) = 0$. These two conditions, of Dirichlet or Neumann type, are equivalent if treated within the Whitham approach, since the corresponding profiles differ only locally near 0, over a characteristic length of order 1.

For intermediate velocities V, the profile is of the type characterized by the arrangement of Riemann invariants displayed in Fig. 4(d): there is a plateau in contact with the piston, then, at its right, a DSW, and finally a plateau corresponding to the right boundary condition, characterized by $\lambda_\pm^R = \frac{1}{2}u_R \pm \sqrt{h_R}$. The plateau in contact with the piston is characterized by a height h_L (unknown at this point) and a velocity $v_L = 0$; hence $\lambda_\pm^L = \pm\sqrt{h_L}$. The constancy of the lower Riemann invariant across the structure of Fig. 4(d) yields $\lambda_-^L = \lambda_-^R$, which fixes the value of $h_L = (\sqrt{h_R} - u_R/2)^2$. The velocities
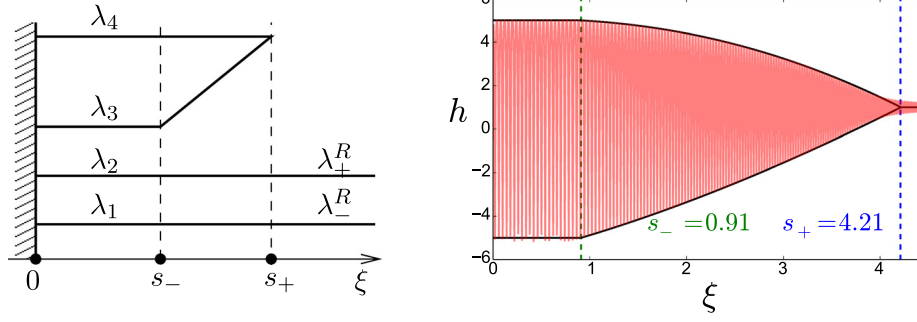
FIG. 10. The piston problem for a velocity $V > 2\sqrt{h_R}$. The left plot displays a sketch of the corresponding arrangement of Riemann invariants. In the rest frame of the piston, the SCW occupies the region $0 < \xi < s_-$, and the DSW the region $s_- < \xi < s_+$. The right plot compares the results of our numerical simulations for $h(x, t)$ with the prediction of Whitham theory. The boundary conditions are $V = 2.5 = -u_R$ and $h_R = 1$. In the numerical approach, the piston is mimicked by a strong repulsive potential.

of the edges of the DSW are determined from (51) and (52). In particular, the boundary between the left plateau and the DSW has a velocity $s_- = \sqrt{h_R} - V/2$. This velocity vanishes when $V = 2\sqrt{h_R}$. For piston velocities V larger than this threshold, the plateau in contact with the piston disappears and the structure of the flow changes: in a good approximation, it is represented by a stationary, non-modulated cnoidal wave (SCW) in contact with the piston. This SCW is connected to its right with a partial DSW, itself connecting to a plateau defined by the right boundary condition. This corresponds to the arrangement of Riemann invariants displayed in Fig. 10.

The fact that the cnoidal wave located in the region $0 < \xi < s_-$ in Fig. 10 is stationary reflects in the relation $\lambda_1 + \lambda_2 + \lambda_3 + \lambda_4 = 0$, which fixes its phase velocity to zero. This yields

$$\lambda_3 + \lambda_4 = -\lambda_1 - \lambda_2 = -u_R = V. \qquad (63)$$

Another condition is obtained by imposing that there is no flux through the piston, and therefore the average flux vanishes: $\langle hu \rangle = 0$ [it is evident that there is no contribution of the last term in the first Eq. (3) to the average flux, since $\langle u_{xx} \rangle \equiv 0$ by virtue of local periodicity]. The relation (63) yields $s_1 = 0$ and Eq. (13) now reads $u = -2\mu$ and $h(\mu) = -s_2 - 2\mu^2$, where $s_2 = \lambda_1\lambda_2 - (\lambda_1 + \lambda_2)^2 + \lambda_3\lambda_4$. Hence we get the condition

$$s_2 \langle \mu \rangle + 2 \langle \mu^3 \rangle = 0, \qquad (64)$$

where $\langle \mu^n \rangle = L^{-1} \oint \frac{1}{2} \mu^n d\mu / \sqrt{-P(\mu)}$. Condition (64) is fulfilled for $s_3 = (\lambda_1 + \lambda_2)(\lambda_3\lambda_4 - \lambda_1\lambda_2) = 0$. Together with (63) this yields a system for the yet unknown quantities λ_3 and λ_4. The obvious solutions are [taking into account the ordering (11)] $\lambda_4 = -\lambda_1$ and $\lambda_3 = -\lambda_2$. Then, in the SCW, the height h oscillates between the two opposite values $\pm 2V\sqrt{h_R}$ and the velocity v between $-V \pm 2\sqrt{h_R}$. The velocities of the edges of the DSW are $s_- = v_3(\lambda_1, \lambda_2, \lambda_3, \lambda_4)$ and $s_+ = v_3(\lambda_1, \lambda_2, \lambda_4, \lambda_4) = 2\sqrt{h_R} + V - h_R/(V + \sqrt{h_R})$. The wavelength of the large amplitude edge of the DSW (at $\xi = s_-$) is given by

$$L = \frac{2K(m^*)}{V}, \quad \text{where} \quad m^* = \frac{4h_R}{V^2} \qquad (65)$$

is the modulus (20) of the elliptic functions; $m^* < 1$ in the present case since $V > 2\sqrt{h_R}$. As is checked in Fig. 10, these predictions are in excellent agreement with the numerical simulations.

Two comments are in order here: first, the numerical simulations show that the cnoidal wave is weakly modulated, and, as suggested in Refs. 12 and 24, it should be more accurately described as a two phase solution. However, as seen in Fig. 10, the modulation is small, and the approximate description of the structure as an SCW is quite accurate. Second, and more important, we have here an example of dynamically stable non-modulated cnoidal wave with large amplitude (h oscillate between ± 5 in the SCW region of Fig. 10). This is quite different from the situation observed in Sec. IV [region (F) in Fig. 5] where an expected SCW resulting from the collision of two DSWs has proven unstable. This example shows that the wave structures in the piston problem may have properties quite different from those arising from the evolution of initial discontinuities.

VI. CONCLUSION

In this paper, we have developed a full classification of the wave patterns evolving dynamically from initial discontinuities according to the Kaup-Boussinesq equation with positive dispersion. At variance with the case of negative dispersion considered in Ref. 12, the classification used here follows closely the one for the nonlinear Schrödinger equation,[18] although there are a number of technical differences caused by the possible negative value of the "height" field and also by different representations of dark and bright "soliton trains" and corresponding changes of the Whitham modulation equations. This common behavior of the positive dispersion Kaup-Boussinesq and the nonlinear Schrödinger equation is related to the common sign of dispersion in both equations and will be clarified in a forthcoming publication.[16]

Our results can find applications as approximations of the dynamics of polarization waves in two-component Bose-Einstein condensates[21] and of magnetic systems with easy-plane anisotropy.[25] Work in this direction is in progress.

[1]R. Courant and K. O. Friedrichs, *Supersonic Flow and Shock Waves* (Interscience Publishers, New York, 1956).

[2]Y. B. Zel'dovich and Y. P. Raizer, *Physics of Shock Waves and High-Temperature Hydrodynamic Phenomena* (Dover Books on Physics, New York, 2002)

[3]A. M. Kamchatnov, *Nonlinear Periodic Waves and Their Modulations—An Introductory Course* (World Scientific, Singapore, 2000).

[4]G. A. El and M. A. Hoefer, "Dispersive shock waves modulation theory," Physica (Amsterdam) **333D**, 11 (2016).

[5]D. J. Korteweg and G. de Vries, "On the change of form of long waves advancing in a rectangular canal, and on a new type of long stationary waves," Philos. Mag. **39**, 422–443 (1895).

[6]T. B. Benjamin and M. J. Lighthill, "On cnoidal waves and bores," Proc. R. Soc. London, A **224**, 448 (1954).

[7]G. B. Whitham, "Non-linear dispersive waves," Proc. R. Soc. London, A **283**, 238–261 (1965).

[8]A. V. Gurevich and L. P. Pitaevskii, "Nonstationary structure of a collisionless shock wave," Zh. Eksp. Teor. Fiz. **65**, 590–604 (1973) [Sov. Phys.-JETP **38**, 291–297 (1974)].

[9]J. Boussinesq, "Essai sur la théorie des eaux courantes," Mém. Prés. Div. Sav. Acad. Sci. Inst. Fr. **23**, 1 (1877).

[10]D. J. Kaup, "A higher-order water-wave equation and the method for solving it," Prog. Theor. Phys. **54**, 396 (1975).

[11]V. B. Matveev and M. I. Yavor, "Solutions presque périodiques er a N-solitons de l'équation hydrodynamique non linéaire de Kaup," Ann. Inst. Henry Poincaré **31**, 25 (1979).

[12]G. A. El, R. H. J. Grimshaw, and M. V. Pavlov, "Integrable shallow-water equations and undular bores," Stud. Appl. Math. **106**, 157 (2001).

[13]G. A. El, R. H. J. Grimshaw, and A. M. Kamchatnov, "Wave breaking and the generation of undular bores in an integrable shallow water system," Stud. Appl. Math. **114**, 395 (2005).

[14]G. A. El, R. H. J. Grimshaw, and A. M. Kamchatnov, "Analytic model for a weakly dissipative shallow-water undular bore," Chaos **15**, 037102 (2005).

[15]The negative dispersion in Eq. (1) corresponds to a "+" sign in front of the third derivative term in the first equation of the system (3).

[16]S. K. Ivanov *et al.*, "The Riemann problem for polarization waves in a two-component Bose-Einstein condensate," (unpublished).

[17]A. V. Gurevich and A. L. Krylov, "Dissipationless shock waves in media with positive dispersion," Sov. Phys. JETP **65**, 944–953 (1987).

[18]G. A. El, V. V. Geogjaev, A. V. Gurevich, and A. L. Krylov, "Decay of an initial discontinuity in the defocusing NLS hydrodynamics," Physica D **87**, 186–192 (1995).

[19]$s_1 = \sum_{i=1}^{4} \lambda_i$, $s_2 = \sum_{i<j} \lambda_i \lambda_j$, $s_3 = \sum_{i<j<k} \lambda_i \lambda_j \lambda_k$ and $s_4 = \Pi_{i=1}^{4} \lambda_i$.

[20]A. M. Kamchatnov, Y.-H. Kuo, T.-C. Lin, T.-L. Horng, S.-C. Gou, R. Clift, G. A. El, and R. H. J. Grimshaw, "Undular bore theory for the Gardner equation," Phys. Rev. E **86**, 036605 (2012).

[21]T. Congy, A. M. Kamchatnov, and N. Pavloff, "Dispersive hydrodynamics of nonlinear polarization waves in two-component Bose-Einstein condensates," SciPost Phys. **1**, 006 (2016).

[22]A. V. Gurevich and A. P. Meshcherkin, "Expanding self-similar discontinuities and shock waves in dispersive hydrodynamics," Zh. Eksp. Teor. Fiz. **87**, 1277–1292 (1984) , [Sov. Phys. JETP **60**, 732–740 (1984)].

[23]G. A. El, "Resolution of a shock in hyperbolic systems modified by weak dispersion," Chaos **15**, 037103 (2005).

[24]R. F. Bikbaev, "Finite-gap attractors and transition processes of the shock-wave type in integrable systems," Zapadn. Nauchno. Semin. POMI **199**, 25 (1992) [J. Math. Sci. **77**, 3033 (1995)].

[25]E. Iacocca, Th. Silva, and M. A. Hoefer, "Breaking of Galilean invariance in the hydrodynamic formulation of ferromagnetic thin films," Phys. Rev. Lett. **118**, 017203 (2017).